LSDSSIMR: Large-Scale Dust Storm Database Based on Satellite Images and Meteorological Reanalysis Data

Cong Bai, *Member, IEEE*, Zhipeng Cai, Xiaomei Yin, and Jinglin Zhang

***Abstract*—In recent years, dust storms have occurred frequently, significantly affecting people's daily lives. Therefore, the detection, monitoring, and early warning of dust storms have a great social significance. Previous methods have mainly been based on atmospheric motion to build physical models for weather forecasting. Although there are many meteorological applications based on deep learning, to the best of authors' knowledge, there is no dust storm database with a high spatiotemporal resolution, which is essential for deep learning methods. Since meteorological satellites can observe the Earth's atmosphere from a spatial perspective at a large scale, in this article, a dust storm database is constructed using multichannel and dust label data from the Fengyun-4 A geosynchronous orbiting satellite, namely the large-scale dust storm database based on satellite images and meteorological reanalysis data (LSDSSIMR), with a temporal resolution of 15 min and a spatial resolution of 4 km from March to May of each year during 2020–2022. Meteorological reanalysis data are added to LSDSSIMR for spatiotemporal prediction methods. Each data file is stored in an HDF5 format, and the final LSDSSIMR contains nearly 5400 HDF5 files. Moreover, some traditional dust detection methods based on spectral analysis are executed as a benchmark.**

***Index Terms*—Database, dust storm, Fengyun-4 A (FY-4A), meteorological reanalysis.**

I. Introduction

THE impact of the Earth's weather systems on human society is becoming increasingly prominent as severe weather disasters have recently become more frequent. These disastrous weather events significantly affect people's daily lives and even have a tremendous negative impact on the social economy [1], [2]. As a type of catastrophic weather phenomenon, dust storms are a symbol of desertification. They are characterized by a high abruptness, short duration, low frequency, great harmfulness, difficulty in monitoring and forecasting, and relatively fixed area. There are three necessary conditions for dust storms to occur: strong winds, drought, and sand sources [3], [4]. In winter and spring, intense convective weather causes strong winds to lift large amounts of sand and dust from dry land (often desert or bare land) when rainfall decreases, reducing the horizontal visibility to less than 4 km. China is one of the countries that is seriously affected by dust storms in the world as the Gobi Desert is located in Mongolia and Inner Mongolia and the Taklamakan Desert is located in northwestern China [5], [6]. Therefore, studying dust storms in China is necessary and of great significance.

It is difficult for ground-based meteorological stations to monitor large-scale disaster weather, such as dust storms and typhoons. However, with the progress of technology, meteorological satellites, such as the Himawari-8/9 [7], Fengyun-4 A (FY-4 A) [8], and moderate resolution imaging spectroradiometer (MODIS) [9] provide more options for meteorological observations [10]. Meteorological satellites obtain the reflectance and brightness temperature in the visible (VIS), near-infrared (NIR), and thermal infrared (TIR) bands, analyze the atmospheric composition and movement, and play an important role in monitoring and predicting large-scale disaster weather [11].

The application of deep learning in the field of remote sensing is increasing [12], [13], [14], [15], [16], [17], [18], which provides a new research direction for meteorological monitoring and weather forecasting. Research on deep learning in the field of dust aerosols is also emerging in an endless stream. Jin et al. [19], used a hybrid algorithm for dust aerosol detection based on radiative transfer simulation and machine learning to achieve better results than physical-based algorithm in detecting tenuous dust aerosols. They analyzed the sensitivity of the TIR channels in the Advanced Himawari Imager (AHI) of the Himawari-8 meteorological satellite to dust aerosols, thus establishing an artificial neural network for dust aerosol detection. In the network, the authors used eight AHI TIR channels, the surface pressure and skin temperature from ERA5 dataset of the European Centre for Medium-Range Weather Forecasts (ECMWF) and the land cover type from MODIS as inputs. The precise profiles of clouds and aerosols derived from the active instrument Cloud-Aerosol Lidar (light detection and ranging) with Orthogonal Polarization

Manuscript received 8 May 2023; revised 7 August 2023 and 14 September 2023; accepted 9 October 2023. Date of publication 18 October 2023; date of current version 14 November 2023. This work was supported in part by the Zhejiang Provincial Natural Science Foundation of China under Grant LR21F020002, in part by the Major Basic Research Projects of Shandong Province under Grant ZR2022ZD32, in part by the Distinguished Young Scholar of Shandong Province under Grant ZR2023JQ025, and in part by the Taishan Scholars Program under Grant tsqn202211290. *(Corresponding author: Xiaomei Yin.)*

Cong Bai and Zhipeng Cai are with the College of Computer Science and Technology, Zhejiang University of Technology, Hangzhou 310023, China (e-mail: congbai@zjut.edu.cn; zhipengcai@zjut.edu.cn).

Xiaomei Yin is with the Beijing Weather Forecast Center, Beijing 100195, China (e-mail: yinxiaomei2010@163.com).

Jinglin Zhang is with the School of Control Science and Engineering, Shandong University, Jinan 250061, China (e-mail: jinglin.zhang@sdu.edu.cn).

Digital Object Identifier 10.1109/JSTARS.2023.3325783

TABLE I
SUMMARY OF DUST-RELATED OR AEROSOL DATA RESOURCES[a]

Name	Region	Data type	Spatial resolution	Temporal resolution	Valiability
AERONET [22]	Global	Aerosol	Distribution of stations[b]	1 h	1998∼present
CALIPSO [23]	Global	Aerosol	5 km	1 d	2006∼present
MODIS AOD [24]	Global	Aerosol optical depth	1 km×1 km	1 d	2000∼present
MERRA-2 AER [25]	Global	Aerosol diagnostics	0.625°×0.5°[c]	1 h	1980∼present
FY-4A	China	Satellite source data and dust scores	4 km×4 km	5 min	2016∼present

[a]Only the best-case scenarios for these resources are counted.
[b]The meteorological stations are discretely distributed, with only a few stations in China, and a large number of data are missing.
[c]In this table, ° denotes latitude and longitude.

(CALIOP) are used as labels. Also, Cui et al. [20], used the autocorrelation model modified by Gaussian kernel function integrated with deep belief network to estimate the concentration of PM2.5. The datasets included hourly average observed surface PM2.5 concentration data from the Environmental Protection Agency, fused aerosol optical depth (AOD) data, and meteorological variables from the ECMWF. The fused AOD data were obtained from Modern-Era Retrospective analysis for Research and Applications, Version 2 (MERRA-2) reanalysis AOD data, AOD products from the geostationary satellite GOES-16, and AOD data from the polar-orbiting satellite Terra MODIS. Deep learning is a data-driven technology that requires a large amount of data as support. Although the field of meteorological research is generating a large amount of meteorological data, how to analyze and reuse these massive amounts of data and how to use these data in deep learning are of great importance. At present, dust data from ground-based meteorological stations operated by the National Oceanic and Atmospheric Administration's (NOAA) National Centers for Environmental Information (NCEI) are available. However, the distribution of these stations is scattered and uneven. Only the weather conditions near the station can be obtained, and large-scale dust storms cannot be monitored. Gkikas et al. [21] obtained global aerosol optical depth MODIS [9] data for 2007–2016 and constructed a dataset. However, the temporal resolution of MODIS data are relatively low, only once or twice a day, and these data cannot be used for continuous monitoring of dust storms in China. The same is true for the Aerosol Robotic Network (AERONET) [22], Cloud-Aerosol Lidar and Infrared Pathfinder Satellite Observation (CALIPSO) [23], and other databases whose temporal and spatial resolutions are given in Table I. Although the spatial resolution is high enough and dust data for the entire Earth can be obtained, they lack pertinence, and the specific observation temporal resolution for China, i.e., hourly or daily, is too low to be used for meteorological observations. To be specific, as for AERONET, the spatial resolution is subjected to the distribution of stations and the temporal resolution is 1 h. In addition, the spatial resolution of CALIPSO is up to 5 km, but its temporal resolution is just 1 d. Therefore, for a particular region, these databases are only able to access data once a day. However, dust storms usually occur over a large area in one day or two. So these databases can only get data once or twice or from just a small area around meteorological station, which is not enough for dust storm forecasting in China.

As far as we know, there is no remote sensing dust storm database with high spatial and temporal resolutions for China. To solve this problem, this article proposes a dust storm database based on the FY-4 A satellite and meteorological reanalysis data obtained from the ECMWF reanalysis (ERA-5) [26] data and the MERRA-2 [27] product from the National Aeronautics and Space Administration (NASA), namely the large-scale dust storm database based on satellite images and meteorological reanalysis data (LSDSSIMR). The FY-4 A is a new generation geostationary orbit meteorological satellite launched by China in 2016. The FY-4 A scans China every five min and the Earth's hemisphere on one side facing the satellite every hour, so the temporal resolution is at the 5-min level. Due to the enormous impact area of a dust storm, a spatial resolution of 4 km is chosen, and each pixel represents the channel value of a 4 km × 4 km area. In order to unify the time interval, LSDSSIMR selects data every 15 min from March to May every year as this is the period of the high occurrence of dust storms. Then, we process data from 13 channels, as well as dust detection Level 2 products, of the FY-4 A and cut the full disk (DISK) or Chinese region (REGC) data to obtain a region with an image size of 640 × 1280.

Meteorological reanalysis data plays an important role in weather system forecast. For example, Huang et al. [28] used the reanalysis data to forecast typhoon and made a good improvement in the experimental results. Similar as typhoon, the motion of dust storm is affected by air pressure, wind speed, and wind direction, which are all included in the reanalysis data. Therefore, the meteorological reanalysis data from the ERA-5 [26] and MERRA-2 [27] products are added as hourly data. The goal is to facilitate the subsequent use of this database in the spatiotemporal forecasting domain.

In general, to solve the problems of these dust-related databases mentioned above, LSDSSIMR has the following characteristics.

1) *Spatial resolution in China:* The spatial resolution of LSDSSIMR is 4 km, and the image size is 640 × 1280. Images of this size cover large parts of China and Mongolia, where dust storms are most frequent, and can be used to monitor large-scale dust storms.
2) *Temporal resolution in China:* The temporal resolution of LSDSSIMR is 15 min. The time frame for data acquisition is March to May of each year during 2020–2022. The data are obtained every 15 min during the day, which means that for a single dust storm, there are dozens of time frames of data to study.
3) *Research on dust storm forecasting:* LSDSSIMR is based on the data of different bands of meteorological satellites, and at the same time the satellite's level 2 product dust

label is added. In addition, the meteorological reanalysis data are added for the forecasting of dust storm.

II. Related Work

In this section, we review several existing dust-related or aerosol data resources: AERONET [22], CALIPSO [23], MODIS AOD [24], and MERRA-2 [25]. These databases aggregate the dust conditions or AOD data from different regions of the world. Table I summarizes and compares the current major dust-related databases with the data source of our proposed database, i.e., the FY-4 A geostationary meteorological satellite.

A. AERONET

Initiated by NASA and expanded through international collaboration, AERONET [22] is a ground-based remote sensing aerosol detection network. It performs an evaluation analysis using almucantar retrievals, providing information about the AOD and other microphysical (such as the volume size distribution) and optical (such as the single scattering albedo) properties [29], [30]. AERONET was originally developed to support spectral radiometer measurements from remote sensing satellites. Measuring the optical properties and precipitable water of atmospheric aerosols from remote sites can overcome the weather influence of ground-based measurements. Each AERONET station is equipped with a CE318 multiband solar photometer, which has eight spectral channels in the VIS and NIR bands, namely 340, 380, 440, 500, 675, 870, 1020, and 1640 nm. The CE318 can track the sun, measure the direct solar radiation, and retrieve the aerosol optical depth and other properties. The hourly measurement data from Beijing Station on Mar. 16, 2021, are shown in Fig. 1(a). After 4:00 (UTC), the AOD measured in each band increased significantly, and a dust storm occurred in northern China on this day, which proves that AERONET can measure the change in the aerosols and reflect the occurrence of a dust storm according to the characteristics of each band. However, as mentioned above, AERONET data are derived from ground-based meteorological stations, which are discretely distributed, so the measurement range depends on the distribution of the meteorological stations. As shown in Fig. 1(b), there were only a dozen weather stations located in China as of 2021: AOE_Baotou, Beijing, BEIJING_2002, Beijing-CAMS, Beijing_PKU, Beijing_RADI, Chen-Kung_Univ, Douliu, Dongsha_Island, EPA-NCU, Erlin, Hong_Kong_PolyU, Hong_Kong_Sheung, Kaohsiung, Lulin, TASA_Taiwan, Taipei_CWB, XiangHe, Xitun, NAM_CO, QOMS_CAS, Cape_Fuguei_Station, and Tai_Ping. This number of stations is not sufficient to monitor large-scale dust storms, and these stations often do not produce data for several days at a time. In general, AERONET can measure the aerosol optical depth of the air in multiple bands and then reflect the dust in the aerosols according to the multiband data and aerosol optical characteristics, but this is useless for some dust storm detection, monitoring, and prediction tasks.

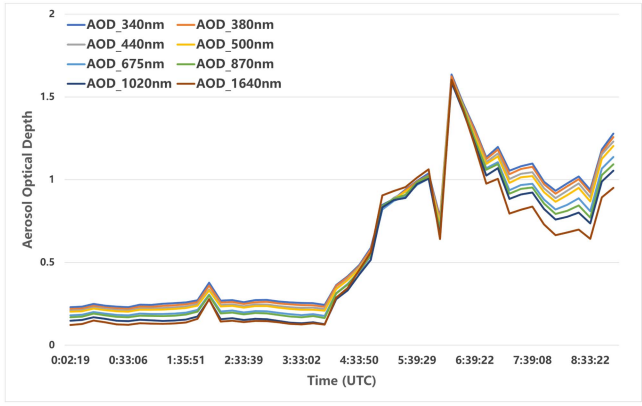

(a)

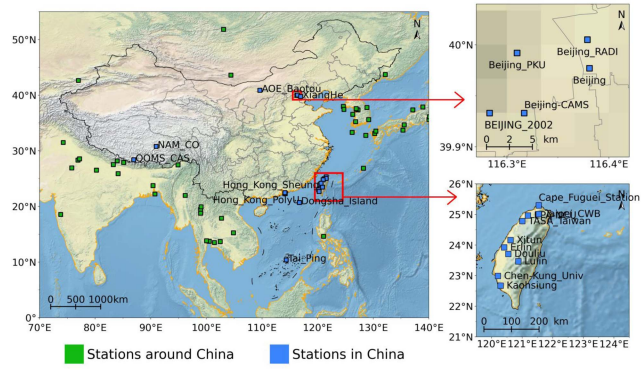

(b)

Fig. 1. (a) Hourly data from a meteorological station in Beijing, Mar. 16, 2021. AERONET diurnal AOD data measured in eight different wavelengths. The AOD index began to rise substantially at around 4:00 (UTC) when a dust storm occurred in Beijing on this day. (b) Distribution map of meteorological stations in and around China in 2021. This map is from the AERONET official website.

B. CALIPSO

The CALIPSO [23], [31] is an Earth-reconnaissance satellite in Sun-synchronous orbit launched by NASA and the Centre National D'Etudes Spatiales in conjunction with CloudSat in 2006. The CALIOP instrument on CALIPSO enables high-resolution aerosol and cloud vertical profiling. CALIPSO circles the Earth in formation with Aqua, Aura, and CloudSat as part of the A Train. CALIPSO monitors aerosols and clouds daily and offers Level 1 products, Level 2 cloud/aerosol layer data, and profile data products. The aerosol product has a spatial resolution of 5 km and passes through the same area every 24 h. As shown in Fig. 2, the vertical feature mask (VFM) aerosol type product of CALIPSO at 19:29 (UTC) on Mar. 15, 2021, shows that there is a dense area of aerosols from (33.8°N, 106.6°E) to (41.2°N, 108.8°E), which is a very large dust storm in northern China that occurred on Mar. 15, 2021. CALIPSO can provide 2-D data for vertical sections of the atmosphere, including a large amount of aerosol and cloud description information. However, the source of the data depends on where the satellite is scanning, and the time resolution is not sufficient. In addition, as shown in the upper part of Fig. 2, from the horizontal perspective, the scanning range of CALIPSO is a line, which cannot be used for large-scale dust storm monitoring.

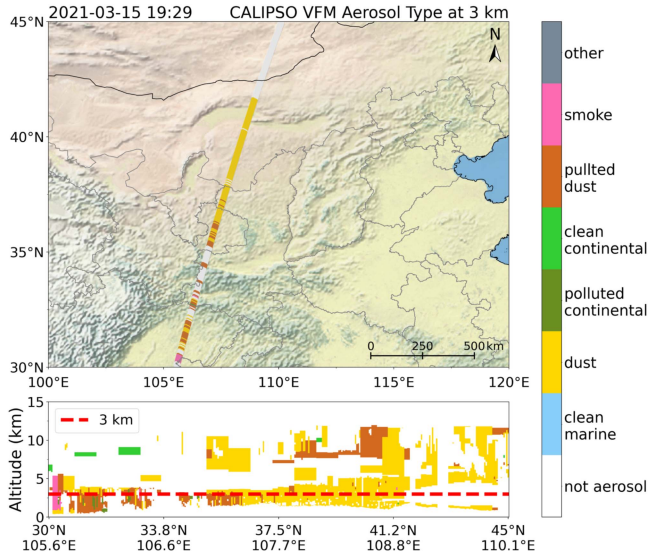

Fig. 2. CALIPSO Level 2 vertical feature mask aerosol type product at 19:29 (UTC) on Mar. 15, 2021. The figure shows the type of aerosol in the vertical profile of the atmosphere along with its geographical location. The upper part of the figure is the scanned trajectory of the satellite (the gray line) and the aerosol type at 3 km. The lower part of the figure is a profile of the atmospheric aerosol types on the scan trajectory.

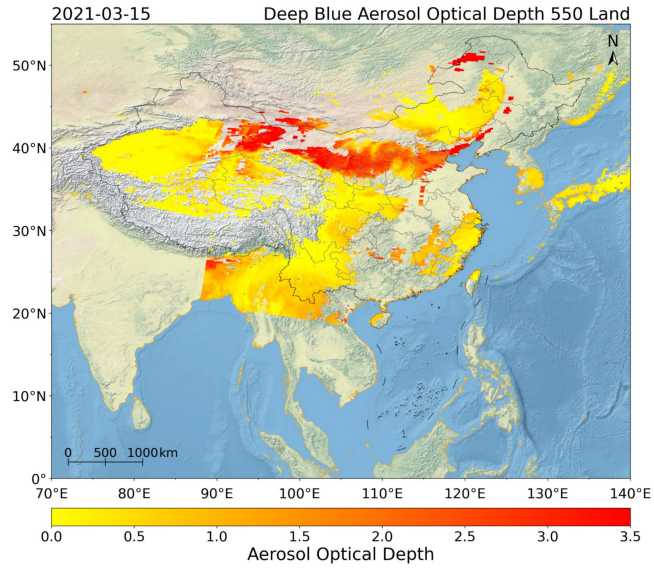

Fig. 3. MODIS aerosol optical depth data acquired on Mar. 15, 2021, China. The deep blue aerosol optical depth increases from yellow to red.

C. MODIS AOD

The Terra and Aqua satellites carry MODISs. The Terra satellite was successfully launched on Dec. 18, 1999, and the Aqua satellite was successfully launched on May 4, 2002. Terra is the Earth observation system (EOS) Ante Meridiem satellite (AM-1), which passes over the equator from north to south at about 10:30 local time. Aqua is the EOS post meridiem satellite (PM-1), which passes over the equator from south to north at about 13:30 local time. The Terra MODIS and Aqua MODIS instruments observe the entire Earth surface every 1–2 days, acquiring data in 36 spectral bands or groups of wavelengths. MODIS has a wide spectral range, covering the full spectrum from 0.4 μm (VIS light) to 14.4 μm (TIR). Multiband data from MODIS can simultaneously provide information reflecting features, such as the land surface conditions, cloud boundaries, cloud properties, ocean water color, phytoplankton, biogeography, chemistry, atmospheric water vapor, aerosols, surface temperature, cloud top temperature, atmospheric temperature, ozone, and cloud top height. It can be used for long-term global observations of the surface, biosphere, solid Earth, atmosphere, and ocean.

MOD04 [24] is a Level 2 aerosol product released by NASA to obtain atmospheric aerosol optical properties, such as the optical depth and size distribution, and the mass concentration in global marine and terrestrial environments. The aerosol optical thickness of a region can be obtained using the deep blue approach [32], [33] for aerosol retrieval at the 10-km scale, and thus, the extent of a dust storm can be obtained. The aerosol optical depth data from MOD04 for the China region on Mar. 15, 2021, are shown in Fig. 3. The red area is the dense aerosol area, that is, the area where a large-scale dust storm broke out in northern China. MODIS is a very common data source in the field of meteorological research [9], [21], [33], [34], [35], [36]. However, like the previously discussed products, the temporal resolution in China is only one day, which is too low to meet the needs of dust storm monitoring.

D. MERRA-2

The MERRA-2 [37] has recorded data since 1980. MERRA-2 is the first long-term global meteorological reanalysis dataset, which includes atmospheric reanalysis data, such as precipitation, aerosol, wind speed, temperature, and radiation data. MERRA-2 has a spatial resolution of 0.5° latitude $\times$ 0.625° longitude and a temporal resolution of up to 1 h. The aerosol reanalysis data in MERRA-2 can be used as the basis for dust storm detection, and the temporal and spatial resolutions also meet our requirements. However, this reanalysis dataset can only be used as training data, not for real-world applications. Due to the low timeliness of the reanalysis data, its release is usually delayed by one or two months, which is not useful for dust storm monitoring and early warning.

III. Database Construction

In this section, the process of constructing the LSDSSIMR is described. This article proposes a database for dust storms from March to May during 2020–2022, with a temporal resolution of 15 min and a spatial resolution of 4 km. The data are saved as HDF5 format files. Each HDF5 file contains satellite multichannel observation Level 1 data and dust detection scoring Level 2 data. The results of traditional spectral analysis dust detection methods, such as brightness temperature adjusted dust index (BADI), infrared difference dust index (IDDI), and normalized difference dust index (NDDI) are added to the LSDSSIMR, which can be used as a benchmark for dust detection in the

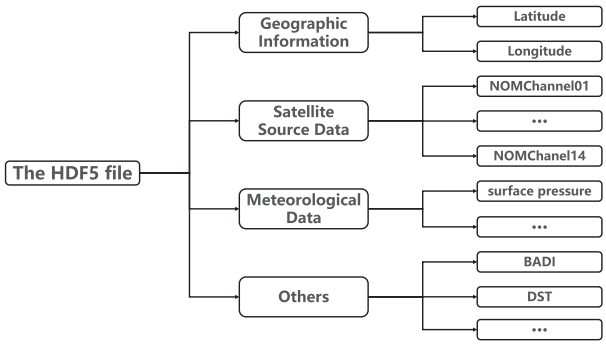

Fig. 4. Architecture of each HDF5 file. There are four groups, with multiple datasets under each group.

future. In addition, the LSDSSIMR includes hourly atmospheric reanalysis data from MERRA-2 [27] and ERA-5 [26]. Based on these data, the LSDSSIMR can be used as a database for detecting, monitoring, and predicting dust storms. The architecture of each HDF5 file is shown in Fig. 4.

A. Data Sources

Many meteorological satellite datasets were investigated as potential data sources, including MODIS, FY-4 A, Himawari-8, and Suomi National Polar-orbiting Partnership/VIS Infrared Imaging Radiometer Suite. LSDSSIMR was designed to monitor and predict dust storms in the Chinese region, so the primary need for LSDSSIMR was to include China and the surrounding area. In addition, a high temporal resolution was also an essential requirement in order to make these data highly usable for spatiotemporal series applications. The high temporal resolution also provided the advantage of expanding the amount of data for a single dust storm, which often lasts only a few days or even a few hours. Dust labels were also a must. Manual annotation is a difficult task if satellite cloud images only have source data and do not have dust labels. In summary, for this large-scale dust storm monitoring dataset within the scope of China, the requirements included a high temporal resolution, multichannel data, suitable spatial resolution, and dust labels. Given the analysis of the database requirements, we focused on the geosynchronous orbit satellite, FY-4 A, launched in 2016 by China.

The primary missions of FY-4 A are to acquire multispectral, high-precision quantitative observations of the Earth's surface, clouds, and atmosphere. FY-4 A is equipped with China's latest generation of Advanced Geostationary Radiation Imager (AGRI), and the scanning area meets all of the requirements. FY-4 A is capable of imaging China and the surrounding areas every 5 min with a maximum spatial resolution of 500 m. The AGRI has 14 channels with a central wavelength ranging from 0.47μm to 13.5μm. In the VIS and NIR bands, the spatial resolution of the AGRI is up to 500 m and is generally 1 km. In the short-wave infrared (SWIR) bands, the spatial resolution is generally 2 km. The spatial resolution of the AGRI is 4 km in the mid-wave infrared (MWIR) and long-wave infrared (LWIR) bands. The detailed information and applications of each band

TABLE II
DETAILED INFORMATION ABOUT EACH CHANNEL FOR THE FY-4 A SATELLITE DATA

Spectral coverage	Spectral bandwidth (μm)	Spatial resolution (km)	Main application
VIS/NIR	0.45∼0.49	1	aerosol, visibility
	0.55∼0.75	0.5∼1	fog, clouds
	0.75∼0.90	1	aerosols, vegetation
SWIR	1.36∼1.39	2	cirrus cloud
	1.58∼1.64	2	cloud, snow
	2.1∼2.35	2∼4	cloud phase, aerosol, vegetation
	3.5∼4.0 (high)	2	clouds, fire, moisture, snow
	3.5∼4.0 (low)	4	land surface
MWIR	5.8∼6.7	4	high water vapor
	6.9∼7.3	4	middle water vapor
LWIR	8.0∼9.0	4	volcanic ash, cloud-top phase
	10.3∼11.3	4	clouds, surface temperature
	11.5∼12.5	4	clouds, low water vapor
	13.2∼13.8	4	clouds, air temperature

of the AGRI are given in Table II. Since FY-4 A data do not continuously contain an image every 5 min, in order to fix the time resolution of the data, the time resolution was set to 15 min. Ultimately, we downloaded FY-4 A Level 1 data and Level 2 dust detection products every 15 min. In addition, to ensure that each cloud image was not too large, and to consider the multichannel imaging status of the AGRI, the spatial resolution was set to 4 km.

The spring (March–May) is a period of frequent dust storms in China. Therefore, the LSDSSIMR was constructed based on the data from March to May for three years (2020–2022). The reason for this is that every year before March, the Northern Hemisphere has just passed the cold winter season. The continuous drought caused by the Mongolian–Siberian High (Asian High) has left much of the China–Mongolia region bare and dry, providing sand sources for the outbreak of dust storms. In addition, the sun starts shining directly on the Northern Hemisphere in March, and the warm Pacific air begins to flow northward. As a result, warm air pushes northward continuously and meets the northern cold air in Mongolia, creating intense convection weather and strong wind conditions that are favorable for dust storms.

B. Processing of Raw Data

The original data could not be used directly as database data, so raw data processing was indispensable. The full disk imaging interval of the FY-4 A is 1 h, and the imaging interval of the Chinese region is 5 min, which leads to an inconsistency in the resolution of the source data, so we needed to cut it. The detailed clipping process of the source data is shown in Fig. 5. The overlapping part of the China region was found from the DISK with a resolution of 2748 × 2748 and the REGC with a resolution of 1092 × 2748, and these two resolutions were cropped to 640 × 1280. As can be seen from Fig. 5, the cropped area covers most of the Chinese landmass, except Hainan, including the Gobi Desert and Taklamakan Desert.

The FY-4 A source data were stored after format conversion from Float to Integer format. The first step was to extract the

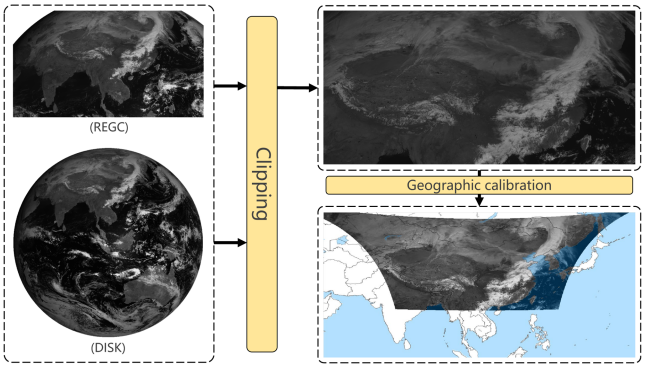

Fig. 5. Same area with a resolution of 640 × 1280 was taken from the source data with two different resolutions. The final geographical calibration shows that this area contains the main dust areas in China and the sand source areas in northern and northwestern China.

float value corresponding to each separately stored integer. In the FY-4 A source files, the 2-D imaging data were stored in Integer format in the datasets named NOMChannel. The multichannel sensor radiation values corresponding to each integer value were stored in the CALChannel datasets in Float format. We extracted this correspondence from the source data and stored it in the database in the Float32 format.

In addition, the geographic information from the FY-4 A was stored separately in the GEO file as row and column numbers. The row and column numbers here were the row and column numbers in a 2748 × 2748 lookup table[1] corresponding to the latitude and longitude of the FY-4 A data. The latitude and longitude information was obtained from the lookup table based on the row and column numbers in the GEO file and was stored in the latitude and longitude datasets in the database. The latitude and longitude datasets were stored together in the geographic information group. In addition, the satellite and solar altitude, azimuth, and other related information for some possible research needs were added to the database. This multichannel information and orientation were stored in the satellite source data group. Moreover, the dust test product (DSD), dust score product (DST), IDDI product (IDDI_BK), and IDDI product with DST (IDDI_DST) in the Level 2 dust detection products were stored in the others group.

C. Meteorological Data

A dust storm is caused by severe convection weather with strong winds, so meteorological information is also necessary when studying the dust storms. According to our research, numerous meteorological reanalysis datasets are available. Among these vast amounts of data, three meteorological data sources were chosen to add to the database. The hourly climate and weather reanalysis data and sources were as follows. Hourly global meteorological station data from the NCEI, ERA-5 [26] hourly climate and weather reanalysis data from the ECMWF, and MERRA-2 [27] atmospheric reanalysis data from NASA.

[1]Download from http://satellite.nsmc.org.cn/PortalSite/StaticContent/DocumentDownload.aspx?TypeID=22

TABLE III
WEATHER OBSERVATION CODES FOR DUST CONDITIONS

Codes	Weather phenomenon
6	Dust or sand hung in the air
7	Dust or sand kicked up by the wind was observed near the station
8	Formation of sand swirls or dust swirls was observed near the station
9	Dust storm was observed near the station
30	Light to moderate dust storms were weakening
31	Light or moderate dust storms did not change significantly
32	Light to moderate dust storms were intensifying
33	Severe dust storms decreased
34	Severe dust storms did not change significantly
35	Severe dust storms weakened or disappeared

a) Meteorological Station Data from NOAA's NCEI: The time interval of the meteorological station data from the NCEI was 3 h, so the meteorological station data were added to the file in the database every 3 h. Data from more than 400 meteorological stations of the global meteorological system in China and Mongolia were selected. We matched the corresponding values in the cloud map grid according to the weather phenomena recorded by the meteorological stations. One of the types of data recorded by the meteorological station was weather phenomenon, denoted by a code. Each code corresponded to a weather phenomenon. The weather phenomenon codes related to sand and dust are given in Table III. These dust-related codes were extracted to match the latitude and longitude of each meteorological station to the longitude and latitude in the database file. The weather phenomenon code for that site's location was stored in an another 2-D array, 640 × 1280. Considering that the longitude and latitude positions of the pixels of our cloud image were discrete and the phenomenon observed by the meteorological station occurred a range of locations, we performed nearest matching according to the location of the meteorological station and assigned the weather phenomenon code within a 5 × 5 range centered on the matched coordinate grid point. Finally, this 2-D array of weather phenomena was stored in Float32 format in the dust with station dataset in the others group.

b) ERA-5 Hourly Climate and Weather Reanalysis Data from ECMWF: ERA-5 [26] is the 5th generation reanalysis dataset from the ECMWF and contains global climate and weather values over the past 40–70 years. Therefore, our data were derived from the ERA-5 hourly data on single levels from 1979 to present dataset. Based on the study of how dust storms move through the atmosphere, several relevant datasets (2 m dew point temperature, mean sea level pressure, skin temperature, surface pressure, 2 m temperature, 10 m U wind component, 10 m V wind component, and total precipitation) were selected from the ERA-5. These datasets were 3-D (24 × 721× 1440), with hour, latitude, and longitude dimensions. Since the database files were 15 min apart, LSDSSIMR only matched these weather data with the files on the hour. In addition, the resolution of these datasets in China was not as high as the resolution of the satellite source files. To solve this problem, nearest neighbor matching was performed on the 721 × 1440 meteorological data based on the latitude and longitude coordinates of the satellite multichannel radiation values for each pixel. That is, the nearest pixel to the longitude and latitude represented by each pixel of the satellite cloud image was found in the longitude and latitude

coordinates of the meteorological data, and the value of the pixel was taken as the value of the satellite cloud image pixel. In this way, the matching of values between the two coordinate systems was achieved. These datasets were stored in the meteorological data group.

c) MERRA-2 Atmospheric Reanalysis Data from NASA: MERRA-2 [27] is an atmospheric reanalysis dataset provided by NASA. As a complement to the ERA-5 [26], the MERRA2_400.inst1_2d_asm_Nx dataset was selected. In addition, several other relevant 3-D datasets (10 m air temperature, 2 m eastward wind, 2m northward wind, eastward wind at 50 m, and northward wind at 50 m) from MERRA-2 were chosen. Nevertheless, unlike the ERA-5, the three dimensions of these datasets were $24 \times 361 \times 576$, and the resolution of the latitude and longitude was somewhat lower than that of the ERA-5. These datasets were stored in the meteorological data group after performing the same procedure performed on the ERA-5 data.

D. Dust Indexes

In addition, to ensure that the database had a benchmark for dust storms, the results of several traditional dust detection methods based on spectral analysis were also added to the others group.

1) *IDDI [38]:* The IDDI uses the brightness temperature depression at 11μm. The band with a center wavelength of 10.8μm is used instead of 11μm in the FY-4 A data, and the following bands are adjusted to the bands of the FY-4 A data. The IDDI is calculated as follows:

$$\mathrm{IDDI} = \mathrm{BT}_{\mathrm{ref}} - \mathrm{BT}, \tag{1}$$

where BT is the brightness temperature, and the subscript ref indicates the maximum value of the brightness temperature within 15 days at that time. The IDDI can be obtained by subtracting the current BT value from the reference BT value. According to this value, the result of whether there is a dust storm or not can be obtained.

2) *NDDI [35]:* Another classical dust index is the NDDI, which uses spectral features in the visible (close to 0.47 μm) and NIR (close to 2.22 μm) bands. The algorithm is expressed as follows:

$$\mathrm{NDDI} = \frac{R_{2.22\mu\mathrm{m}} - R_{0.47\mu\mathrm{m}}}{R_{2.22\mu\mathrm{m}} + R_{0.47\mu\mathrm{m}}} \tag{2}$$

where R is the reflectance. In the NIR spectrum (i.e., 0.4–2.5 μm), the spectral characteristics of dust in the reflection spectrum generally exhibit an upward trend and reach a peak at about 2.22 μm. In contrast, the highest point of a cloud is about 0.47 μm, and the lowest point is about 2.22 μm. Thus, the NDDI is generally positive for dust pixels, negative for clouds, and close to zero for clear sky cases. This indicates that the NDDI can distinguish dust storms from clouds.

3) *BADI [34]:* The BADI is based on the principle that brightness temperature difference (BTD) of 11 μm and 12 μm (BTD^{11-12}) can detect the dust range, and BTD^{3-11} can indicate the dust density. The BADI is calculated using (3). The BTD method is enhanced by synthesizing two BTDs ($\mathrm{BTD}_{3.72\,\mu\mathrm{m}-10.8\,\mu\mathrm{m}}$ and $\mathrm{BTD}_{10.8\,\mu\mathrm{m}-12.0\,\mu\mathrm{m}}$). The higher the value of $\mathrm{BTD}_{3.72\,\mu\mathrm{m}-10.8\,\mu\mathrm{m}}$ is, the higher the dust density is.

$$\mathrm{BADI} = \frac{2}{\pi} \times \arctan\left(\frac{\mathrm{BDI}}{\mathrm{BDI}_{0.95}}\right). \tag{3}$$

The BDI is calculated using (4). The $\mathrm{BDI}_{0.95}$ is the 95th percentile of the BDI. The closer BADI is to 1, the more likely it will be dust.

$$\mathrm{BDI} = \left(\mathrm{BTD}_{3.72-10.8}\right)^2 \times \mathrm{BTD}_{12.0-10.8}. \tag{4}$$

4) *DRBTD [39]:* An automatic dust detection algorithm with dynamic thresholds is based on the dynamic reference brightness temperature difference (DRBTD) [39]. The algorithm integrates some channels related to dust characteristics and adopts the dynamic threshold method as follows:

$$\mathrm{Dust} = \begin{cases} \mathrm{BTD}_{10.8-12.0} < \mathrm{RBTD}_{10.8-12.0} + a \\ \mathrm{BTD}_{8.5-10.8} > \mathrm{RBTD}_{8.5-10.8} + b \\ \mathrm{BTD}_{3.7-10.8} > \mathrm{RBTD}_{3.7-10.8} + c \end{cases}. \tag{5}$$

In (5), RBTD is the reference brightness temperature difference value under clear sky conditions. The reference brightness temperature at a particular moment in a clear sky is the brightness value of each channel when the brightness value in the 10.8-μm band is the maximum at the same time each day for the past 15 days. a, b, and c are three thresholds, and they take different values in different cases.

Taking the DST product as the ground truth, four indicator, i.e., the accuracy, kappa coefficient, recall, and precision, were used to evaluate the correctness of these different dust analysis results. These metrics were computed directly while processing the data, and were stored in the others group.

IV. Experiments

To confirm that this remote sensing database can be used for dust storm research, we perform several semantic segmentation methods for dust storm detection. In this section, several commonly used semantic segmentation methods are briefly introduced. Then, the details of the experimental design and network parameters, as well as some evaluation metrics, are explained. Finally, a brief analysis and discussion of the experimental results are presented.

A. Semantic Segmentation Methods

By treating places with dust storms as dust and places without dust storms as background, such a problem as dust storm detection becomes a semantic segmentation problem. We chose U-Net [40], UNet++ [41], Attention U-Net [42], and the newer TransUNet [43] and Swin-Unet [44], which apply the transformer [45] as the experimental methods.

U-Net [40] was originally created to solve a problem in medical image segmentation. Since then, it has been widely

used in many applications of semantic segmentation due to its well-behaved effect. U-Net has a simple but effective encoder–decoder structure. The encoder is responsible for the feature extraction, while the decoder recovers the original resolution and outputs the segmentation result.

UNet++ [41] alleviates the unknown network depth by efficiently integrating U-Nets with different depths. These variant U-Nets can partially share the same encoder while performing colearning through deep supervision. The authors redesigned the skip-connection to aggregate the different features at the semantic scale in the decoder sub-network, resulting in highly flexible feature fusion and pruning schemes.

The Attention U-Net [42] was inspired by the attention approach proposed in [46]. The Attention U-Net is designed to address the excessive focus on global features in previous work. Thanks to the attention mechanism, irrelevant regions in the input image can be suppressed while highlighting salient features in specific local regions. Attention gates can be easily integrated into standard convolution neural network (CNN) architectures, such as the U-Net model [40] with minimal additional computational effort, resulting in significant improvements in the model sensitivity and prediction accuracy. In dust storm detection, we need to pay more attention on the dusty areas and less attention on the background areas.

The TransUNet [43] has the advantages of both the transformer and U-Net. Due to the tremendous success of Vision Transformer (ViT) [47], transformer's adoption in the imaging field has exploded. CNNs cannot make good use of global information due to the presence of perceptual fields, but they can extract local information very well. The self-attention (SA) structure has advantages for global information extraction but is not good for local detail information extraction. Therefore, TransUNet combines the advantages of a CNN and SA by combining ViT [47], ResNet50 [48], and skip-connection, which adopts the encoder structure of Transformer in the encoder part of U-Net in order to extract the features better.

Motivated by the success of the Swin Transformer [49], Swin-Unet [44] was proposed to implement 2-D medical image segmentation using transformer. Swin-Unet is the first pure transformer-based U-architecture with a skip-connection symmetric encoder–decoder system. SA from local to global scales is implemented in the encoder. In the decoder, the global features are upsampled to the input resolution for the corresponding pixel-level segmentation prediction.

B. Experimental Environment and Parameter Settings

All of the experiments were implemented using a station equipped with four NVIDIA A6000 graphics processing units (GPUs) with 48 GB of memory per GPU. The data for 2020 and 2021 were used as the training set. The data of March 2022 were used as the validation set and the data for April and May 2022 were used as the testing set. Finally, the size of the training set was 3923, the size of the validation set was 440, and the size of the testing set was 1045. Based on the main application of each band in Table II and some formulas in Dust Indexes III-D, six bands of satellite L1 data (0.47, 0.65, 3.72, 8.5, 10.8, and 12.0 μm) were selected as the input data and the Level 2 product DST was used as the label. The DST was converted to a binary image. The values in the DST that were greater than or equal to 12 were filled with 1, and those that were less than 12 were filled with 0, where 1 indicates a dust area and 0 indicates a dust-free area.

TABLE IV
TRAINING PARAMETERS FOR EACH MODEL

Models	Batch size	Epoch	Optimizer	Learning rate
U-Net	32	200	AdamW	0.001
UNet++	32	200	AdamW	0.001
Attention U-Net	32	200	AdamW	0.001
TransUNet	32	200	AdamW	0.001
Swin-Unet	64	200	AdamW	0.0001

The input image size was set to 448 $\times$ 896 cropped from the original image, both width and height are integer multiples of the image size 224 commonly used in ViT [47]. We also performed simple image enhancement via random horizontal-vertical flipping and rotation at random angles. All models were randomly initialized before the training. The other parameters were set according to Table IV. We chose the loss function of adding the dice loss and cross entropy loss, which is more common in semantic segmentation. The loss function is expressed as follows:

$$\text{loss} = \alpha \times \text{DiceLoss} + (1-\alpha) \times \text{CELoss}, \tag{6}$$

where α is the loss weight.

The weight decay was set to 0.0001 for the AdamW method. We chose cosine annealing as the update method for the learning rate because the loss function is difficult to train if dice loss is added.

C. Evaluation Metrics

The evaluation metrics commonly used in the field of semantic segmentation include the dice coefficient, intersection over union (IoU), recall, precision, and kappa coefficient. We treated the dust storm detection as a pixel-level binary classification problem and converted the detection results and the ground truth into 0/1 matrices. Then, we computed the true positive (TP, detection=1, truth=1), false positive (FP, detection=1, truth=0), false negative (FN, detection=0, truth=1), and true negative (TN, detection=0, truth=0). The five evaluation metrics, except the kappa coefficient were defined as follows:

$$\text{DiceCoefficient} = \frac{2\text{TP}}{\text{TP+FP+TN} + \text{FN}}$$

$$\text{IoU} = \frac{\text{TP}}{\text{TP+FP+FN}}$$

$$\text{Recall} = \frac{\text{TP}}{\text{TP+FN}}$$

$$\text{Precision} = \frac{\text{TP}}{\text{TP+FP}}.$$

The kappa coefficient is biased to the problem of an unbalanced sample number, and it is used as an indicator for the consistency test and can also be used to measure the

TABLE V
EXPERIMENTAL RESULTS OF FIVE SEMANTIC SEGMENTATION METHODS FOR DUST STORM DETECTION IN LSDSSIMR

Models	Dice	Kappa	IoU	Recall	Precision
U-Net	0.8143	0.8132	0.7216	0.7710	**0.9076**
UNet++	0.8149	0.8137	0.7202	0.7979	0.8680
Attention U-Net	**0.8366**	**0.8356**	**0.7490**	**0.8063**	0.9047
TransUNet	0.7059	0.7039	0.5862	0.6894	0.7798
Swin-Unet	0.7566	0.7547	0.6442	0.7461	0.8120
BADI(mean)	0.0106	0.2671	0.1738	0.4289	0.2475
BADI(max)	0.0408	0.7294	0.5805	0.9332	0.7744
DRBTD(mean)	0.0075	0.0948	0.0614	0.3340	0.1022
DRBTD(max)	0.1059	0.6331	0.4676	1.0000	0.6758

The bold entities indicate the best result among the five indicators.

effect of the classification. $\mathrm{OA} = \frac{\mathrm{TP}+\mathrm{TN}}{\mathrm{TP}+\mathrm{TN}+\mathrm{FP}+\mathrm{FN}}$, and $\mathrm{AC} = \frac{(\mathrm{TP}+\mathrm{FP})\times(\mathrm{TP}+\mathrm{FN})+(\mathrm{FN}+\mathrm{TN})\times(\mathrm{FP}+\mathrm{TN})}{N\times N}$, where N is the total number of samples, and $\mathrm{KappaCoefficient} = \frac{\mathrm{OA}-\mathrm{AC}}{1-\mathrm{AC}}$. We used these five metrics to evaluate the results of the binary classification experiments for the dust storm detection.

D. Results and Analysis

Table V gives the mean experimental results of the five semantic segmentation methods for dust storm detection based on the testing set in LSDSSIMR. According to the main evaluation metrics, such as the dice coefficient, kappa coefficient, and IoU, the Attention U-Net yielded the best results among the five methods. Because U-Net, UNet++, and Attention U-Net become more complex, the model can better grasp the relationship among the input channels and get better results. TransUNet and Swin-Unet both have more complex models with transformer, but their experimental performance is lower. We believe that this is because binary classification is a simple task and transformer is a complex model, and complex models often perform worse on simple tasks than simpler models do. Thanks to the shifted window mechanism [49], Swin-Unet can better obtain the information association in different patches of the image, thus obtaining better results than TransUNet. According to Cohen's suggestion [50], the kappa coefficient results were interpreted as follows: values of $\leq$0 indicate no agreement, values of 0.01–0.20 indicate no to slight agreement, values of 0.21–0.40 indicate fair agreement, values of 0.41–0.60 indicate moderate agreement, values of 0.61–0.80 indicate substantial, and values of 0.81–1.00 indicate almost perfect agreement. For the results of the different methods, the kappa coefficients reached 0.7–0.84, i.e., substantial to almost perfect agreement. This demonstrates that it is feasible to detect dust storms using semantic segmentation methods.

In addition, we believe that the recall and precision metrics are not very meaningful in this task. Take the result from 04:00 on Apr. 27, 2022, as an example. The original confusion matrix for this result is as follows:

$$\begin{bmatrix} & \mathrm{truth}(1) & \mathrm{truth}(0) \\ \mathrm{detection}(1) & 11125 & 1053 \\ \mathrm{detection}(0) & 2343 & 386887 \end{bmatrix}.$$

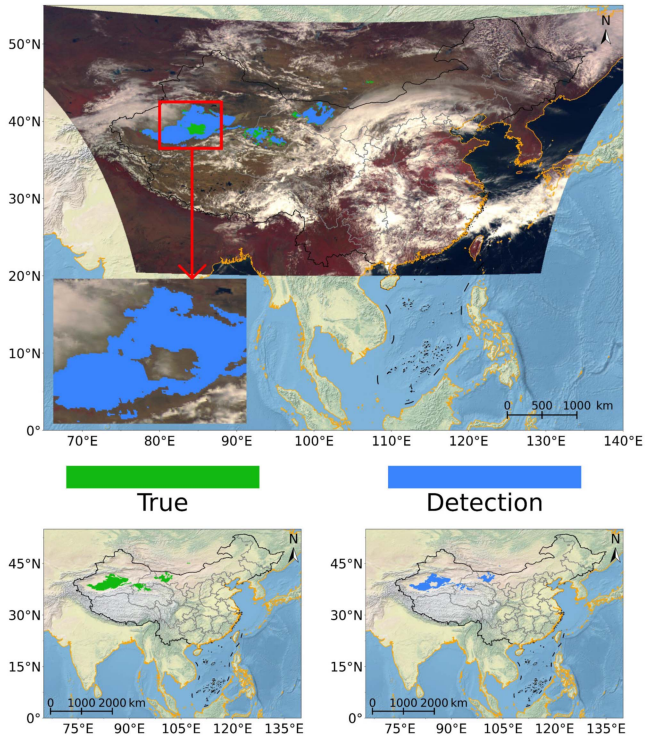

Fig. 6. One result of the Attention U-Net on Apr. 27, 2022 at 04:00:00 (UTC). The green area is the true dust storm, and the blue area is the detected dust storm.

The precision value is 0.9135 ($\frac{11125}{11125+1053} \approx 0.9135$) and the recall value is 0.8260 ($\frac{11125}{11125+2343} \approx 0.8260$). If the whole image is a dust region, the confusion matrix of the truth value and the detection value of the result is shown as follows:

$$\begin{bmatrix} & \mathrm{truth}(1) & \mathrm{truth}(0) \\ \mathrm{detection}(1) & 13468 & 387940 \\ \mathrm{detection}(0) & 0 & 0 \end{bmatrix}.$$

According to the definition of recall, the value will reach 1 ($\frac{13468}{13468+0} = 1$) because FP values are not considered. This is why the recall value of DRBTD(max) reaches 1.0, which actually means that the detected dust region includes all of the true region. If the detected dust storm region is only a small part of the truth, the confusion matrix is shown as follows:

$$\begin{bmatrix} & \mathrm{truth}(1) & \mathrm{truth}(0) \\ \mathrm{detection}(1) & 3004 & 201 \\ \mathrm{detection}(0) & 10464 & 387739 \end{bmatrix}.$$

According to the definition of precision, the value will be 0.9373 ($\frac{3004}{3004+201} \approx 0.9373$), which is higher than 0.9135 because FN values are not considered. This is the reason why the precision results are high for each model in Table V. The above two special cases can make the results really fascinating, but the reality is that all dust storm region and smaller dust storm region are not the best case or even the worst case. What we are most concerned about is whether the difference between the final detection result and the truth is small. These two metrics have very high values, but the results are very different from the truth.

The four rows on the bottom of Table V list the experimental results of the traditional methods. The average results of the traditional methods are much worse than those of the deep learning methods, which also demonstrates that the use of deep learning methods for dust storm detection and early warning is a promising research direction.

One segmentation result of the Attention U-Net is shown in Fig. 6, in which the results for the detection and true phenomenon mostly coincide. In the red rectangle, parts of the dust storm are not detected but actually exist. This is because there was cloud occlusion in the satellite image, and the dust storm was below the clouds. The red arrow in Fig. 6 points to the part where there were clouds. We denoised and filled the true (ground truth) dust storm area, based on the fact that dust storms occur over large areas, so the true area in green in Fig. 6 is shown as a dust storm area in this location.

V. Conclusion

In this study, the requirements for dust storm detection, monitoring, and early warning in the Chinese region were analyzed, and the FY-4 A was chosen as the data source for constructing a dust storm database named LSDSSIMR. The satellite data with dust labels (DST) were processed, and the relevant meteorological data were added. LSDSSIMR spans from March to May during 2020–2022. As a result, LSDSSIMR contains nearly 5400 HDF5 files, each with a resolution of 640×1280. In order to make the database useful for dust monitoring and prediction in the future, many meteorological reanalysis data were added. In this way, the data types included in LSDSSIMR were remote sensing images and reanalysis data at different times. These data at different times can capture the motion characteristics of the atmosphere and aerosol, and then some specific methods can use these characteristics to forecast dust storm. Based on the dust storm forecasting, we can make more preparations in advance to protect life and economic security from dust storm. In addition, we evaluated several semantic segmentation methods using five evaluation metrics in the LSDSSIMR. The experiments yielded some substantial results, which can be used as a baseline for related further research. The LSDSSIMR can be downloaded from GitHub: https://github.com/Zjut-MultimediaPlus.

V. Acknowledgment

The authors would like to thank the ECMWF for providing the ERA-5 [26] reanalysis product, NASA for providing the MERRA-2 [27] product, and the NCEI of NOAA for providing the meteorological station data.

References

[1] G. Deng, H. Chen, and S. Wang, "Risk assessment and prediction of rainstorm and flood disaster based on Henan province, China," *Math. Problems Eng.*, vol. 2022, pp. 1–17, Feb. 2022.

[2] Z. Tao and L. Han, "Emergency response, influence and lessons in the 2021 compound disaster in Henan province of China," *Int. J. Environ. Res. Public Health*, vol. 19, 2022, Art. no. 488.

[3] K. Gui et al., "Two mega sand and dust storm events over northern China in March 2021: Transport processes, historical ranking and meteorological drivers," *Atmospheric Chem. Phys.*, vol. 12, 2021.

[4] K. Gui et al., "Record-breaking dust loading during two mega dust storm events over northern China in Mar. 2021: Aerosol optical and radiative properties and meteorological drivers," *Atmospheric Chem. Phys.*, vol. 22, no. 12, pp. 7905–7932, 2022.

[5] L. Yang et al., "Characteristics of dust events in China from 2015 to 2020," *Atmosphere*, vol. 12, no. 8, 2021, Art. no. 952.

[6] A. Aili, H. Xu, T. Kasim, and A. Abulikemu, "Origin and transport pathway of dust storm and its contribution to particulate air pollution in northeast edge of Taklimakan Desert, China," *Atmosphere*, vol. 12, 2021, Art. no. 113.

[7] K. Bessho et al., "An introduction to Himawari-8/9– Japan's new-generation geostationary meteorological satellites," *J. Meteorological Soc. Jpn.*, vol. 94, pp. 151–183, 2016.

[8] J. Yang, Z. Zhang, C. Wei, F. Lu, and Q. Guo, "Introducing the new generation of Chinese geostationary weather satellites, Fengyun-4," *Bull. Amer. Meteorological Soc.*, vol. 98, pp. 1637–1658, 2017.

[9] V. V. Salomonson, W. L. Barnes, P. W. Maymon, H. Montgomery, and H. Ostrow, "MODIS: Advanced facility instrument for studies of the earth as a system," *IEEE Trans. Geosci. Remote Sens.*, vol. 27, pp. 145–153, Mar. 1989.

[10] P. Bauer, A. J. Thorpe, and G. Brunet, "The quiet revolution of numerical weather prediction," *Nature*, vol. 525, pp. 47–55, 2015.

[11] S. Kalluri, C. Zou, and L. E. Flynn, "Applications of joint polar satellite system data and products for severe weather events and climate monitoring," in *Proc. IEEE Int. Geosci. Remote Sens. Symp.*, 2021, pp. 695–698.

[12] J. Zhang, P. Liu, F. Zhang, and Q. Song, "CloudNet: Ground-based cloud classification with deep convolutional neural network," *Geophysical Res. Lett.*, vol. 45, pp. 8665–8672, 2018.

[13] C. Bai, M. Zhang, J. Zhang, J. Zheng, and S. Chen, "LSCIDMR: Large-scale satellite cloud image database for meteorological research," *IEEE Trans. Cybern.*, vol. 52, no. 11, pp. 12538–12550, Nov. 2022.

[14] C. Bai, D. Zhao, M. Zhang, and J. Zhang, "Multimodal information fusion for weather systems and clouds identification from satellite images," *IEEE J. Sel. Topics Appl. Earth Observ. Remote Sens.*, vol. 15, pp. 7333–7345, 2022, doi: 10.1109/JSTARS.2022.3202246.

[15] C. Huang, C. Bai, S. Chan, and J. Zhang, "MMSTN: A. multi-modal spatial-temporal network for tropical cyclone short-term prediction," *Geophysical Res. Lett.*, vol. 49, 2022, Art. no. e2021GL096898.

[16] C. Bai, F. Sun, J. Zhang, Y. Song, and S. Chen, "Rainformer: Features extraction balanced network for radar-based precipitation nowcasting," *IEEE Geosci. Remote Sens. Lett.*, vol. 19, 2022, Art. no. 4023305.

[17] D. Zhao, Q. Wang, J. Zhang, and C. Bai, "Mine diversified contents of multispectral cloud images along with geographical information for multilabel classification," *IEEE Trans. Geosci. Remote Sens.*, vol. 61, 2023, Art. no. 4102415. [Online]. Available: https://doi.org/10.1109/TGRS.2023.3270204

[18] W. Li, F. Zhang, H. Lin, X. Chen, J. Li, and W. Han, "Cloud detection and classification algorithms for Himawari-8 imager measurements based on deep learning," *IEEE Trans. Geosci. Remote Sens.*, vol. 60, 2022, Art. no. 4107117. [Online]. Available: https://api.semanticscholar.org/CorpusID:247032794

[19] J. Jin, F. Zhang, W. Li, Q. Wu, L. Mei, and L. Chen, "A hybrid algorithm for dust aerosol detection: Integrating forward radiative transfer simulations and machine learning," *IEEE Trans. Geosci. Remote Sens.*, vol. 61, 2023, Art. no. 4104715. [Online]. Available: https://api.semanticscholar.org/CorpusID:261178729

[20] Q. Cui, F. Zhang, S. Fu, X. Wei, Y. Ma, and K. Wu, "High spatiotemporal resolution PM2.5 concentration estimation with machine learning algorithm: A case study for wildfire in california," *Remote. Sens.*, vol. 14, 2022, Art. no. 1635. [Online]. Available: https://api.semanticscholar.org/CorpusID:247905601

[21] A. Gkikas et al., "ModIs dust AeroSol (MIDAS): A global fine-resolution dust optical depth data set," *Atmospheric Meas. Techn.*, vol. 14, no. 1, pp. 309–334, 2021.

[22] B. N. Holben et al., "AERONET-A federated instrument network and data archive for aerosol characterization," *Remote Sens. Environ.*, vol. 66, pp. 1–16, 1998.

[23] D. M. Winker et al., "Overview of the CALIPSO mission and CALIOP data processing algorithms," *J. Atmospheric Ocean. Technol.*, vol. 26, pp. 2310–2323, 2009.

[24] R. Levy et al., "MODIS atmosphere L2 aerosol product," NASA MODIS Adaptive Processing System, Goddard Space Flight Center USA, 2015.

[25] "MERRA-2 tavg1_2d_aer_Nx: 2d, 1-hourly, time-averaged, single-level, assimilation, aerosol diagnostics V5.12.4, Global Modeling and Assimilation Office (GMAO)," Greenbelt, MD, USA: *Goddard Space Flight Center Distrib. Act. Archive Center (GSFC DAAC)*, 2015. Accessed: Feb. 17, 2023, doi: 10.5067/KLICLTZ8EM9D.

[26] H. Hersbach et al., "ERA5 hourly data on single levels from 1940 to present," *Copernicus Climate Change Service (C3S) Climate Data Store (CDS)*, vol. 10, 2018. Accessed: Feb. 17, 2023.

[27] "MERRA-2 inst1_2d_asm_Nx: 2d, 1-Hourly, instantaneous, single-level, assimilation, single-level diagnostics V5.12.4, global modeling and assimilation office (GMAO)," Greenbelt, MD, USA: *Goddard Space Flight Center Distrib. Act. Archive Center (GSFC DAAC)*, 2015. Accessed: Feb. 17, 2023, doi: 10.5067/3Z173KIE2TPD). [Online]. Available: https://gmao.gsfc.nasa.gov/reanalysis/MERRA-2/

[28] C. Huang, C. Bai, S. Chan, J. Zhang, and Y. Wu, "MGTCF: Multi-generator tropical cyclone forecasting with heterogeneous meteorological data," *Proc. AAAI Conf. Artif. Intell.*, vol. 37, no. 4, pp. 5096–5104, Jun. 2023. [Online]. Available: https://ojs.aaai.org/index.php/AAAI/article/view/25638

[29] O. Dubovik and M. D. King, "A flexible inversion algorithm for retrieval of aerosol optical properties from sun and sky radiance measurements," *J. Geophysical Research, Atmospheres*, vol. 105, no. D16, pp. 20673–20696, 2000.

[30] O. Dubovik et al., "Application of spheroid models to account for aerosol particle nonsphericity in remote sensing of desert dust," *J. Geophysical Research, Atmospheres*, vol. 111, no. D11, 2006, doi: 10.1029/2005JD006619.

[31] D. M. Winker, J. R. Pelon, and M. P. McCormick, "CALIPSO Mission: Spaceborne Lidar for Observation of Aerosols and Clouds," in *Lidar Remote Sensing for Industry and Environment Monitoring III*, vol. 4893. Bellingham, WA, USA: SPIE, 2003, pp. 1–11.

[32] N. C. Hsu, S.-C. Tsay, M. D. King, and J. R. Herman, "Aerosol properties over bright-reflecting source regions," *IEEE Trans. Geosci. Remote Sens.*, vol. 42, no. 3, pp. 557–569, Mar. 2004.

[33] A. M. Sayer, N. Hsu, C. Bettenhausen, and M.-J. Jeong, "Validation and uncertainty estimates for MODIS collection 6 "deep blue" aerosol data," *J. Geophysical Research, Atmospheres*, vol. 118, no. 14, pp. 7864–7872, 2013.

[34] H. Yue, C. He, Y. Zhao, Q. Ma, and Q. Zhang, "The brightness temperature adjusted dust index: An improved approach to detect dust storms using MODIS imagery," *Int. J. Appl. Earth Obs. Geoinformation*, vol. 57, pp. 166–176, 2017.

[35] J. J. Qu, X. Hao, M. C. Kafatos, and L. Wang, "Asian dust storm monitoring combining terra and aqua MODIS SRB measurements," *IEEE Geosci. Remote Sens. Lett.*, vol. 3, pp. 484–486, Oct. 2006.

[36] W. P. Menzel et al., "MODIS global cloud-top pressure and amount estimation: Algorithm description and results," *J. Appl. Meteorol. Climatol.*, vol. 47, pp. 1175–1198, 2008.

[37] R. Gelaro et al., "The modern-era retrospective analysis for research and applications, version 2 (MERRA-2)," *J. Climate*, vol. 30, no. 14, pp. 5419–5454, 2017.

[38] M. Legrand, A. Plana-Fattori, and C. N'doume, "Satellite detection of dust using the IR imagery of meteosat: 1. infrared difference dust index," *J. Geophysical Res.*, vol. 106, pp. 18251–18274, 2001.

[39] Y. Liu, R. Liu, and X. Cheng, "Dust detection over desert surfaces with thermal infrared bands using dynamic reference brightness temperature differences," *J. Geophysical Research, Atmospheres*, vol. 118, pp. 8566–8584, 2013.

[40] O. Ronneberger, P. Fischer, and T. Brox, "U-Net: Convolutional networks for biomedical image segmentation," in *Proc. 18th Int. Conf. Med. Image Comput. Comput.-Assisted Intervention*, 2015, pp. 234–241. [Online]. Available: https://doi.org/10.1007/978-3-319-24574-4_28

[41] Z. Zhou, M. M. R. Siddiquee, N. Tajbakhsh, and J. Liang, "UNet : A nested U-net architecture for medical image segmentation," in *Proc. 4th Int. Workshop Deep Learn. Med. Image Anal. Multimodal Learn. Clin. Decis. Support*, 2018, pp. 3–11.

[42] O. Oktay et al., "Attention U-net: Learning where to look for the pancreas," in *Proc. Int. Conf. Med. Imag. Deep Learn.*, 2018, doi: 10.48550/arXiv.1804.03999.

[43] J. Chen et al., "TransUNet: Transformers make strong encoders for medical image segmentation," *CoRR*, vol. abs/2102.04306, 2021.

[44] H. Cao et al., "Swin-UNet: UNet-like pure transformer for medical image segmentation," in *Proc. Comput. Vis.-ECCV Workshops-Tel Aviv*, in Lecture Notes in Computer Science, L. Karlinsky, T. Michaeli, and K. Nishino, Eds., Israel: Springer, Oct. 23–27, 2022, vol. 13803, pp. 205–218.

[45] A. Vaswani et al., "Attention is all you need," in *Proc. Adv. Neural Inf. Process. Syst. 30: Annu. Conf. Neural Inf. Process. Syst.*, I. Guyon, U. V. Luxburg, S. Bengio, H. Wallach, R. Fergus, S. Vishwanathan, and R. Garnett, Eds., Long Beach, CA, USA: Curran Associates, Inc., Dec. 4–9, 2017, pp. 5998–6008.

[46] S. Jetley, N. A. Lord, N. Lee, and P. H. S. Torr, "Learn to pay attention," in *Proc. 6th Int. Conf. Learn. Representations*, Vancouver, BC, Canada, Apr. 30/May 3, 2018.

[47] A. Dosovitskiy et al., "An image is worth 16x16 words: Transformers for image recognition at scale," in *Proc. 9th Int. Conf. Learn. Representations*, May 3-7, 2021. [Online]. Available: https://openreview.net/forum?id=YicbFdNTTy

[48] K. He, X. Zhang, S. Ren, and J. Sun, "Deep residual learning for image recognition," in *Proc. IEEE Conf. Comput. Vis. Pattern Recognit.*, 2015, pp. 770–778.

[49] Z. Liu et al., "Swin transformer: Hierarchical vision transformer using shifted windows," in *Proc. IEEE/CVF Int. Conf. Comput. Vis.*, 2021, pp. 9992–10002.

[50] J. Cohen, "A coefficient of agreement for nominal scales," *Educ. Psychol. Meas.*, vol. 20, no. 1, pp. 37–46, 1960.